



## Molecular structure and phase behaviour of hairy-rod polymers

Title	Molecular structure and phase behaviour of hairy-rod polymers
Author(s)	Cheung, David L.;Troisi, Alessandro
Publication Date	2009
Publisher	Royal Society of Chemistry
Repository DOI	<a href="https://doi.org/10.1039/B818428C">10.1039/B818428C</a>

# Molecular structure and phase behaviour of hairy-rod polymers

David L. Cheung and Alessandro Troisi

<sup>a</sup> Department of Chemistry and Centre for Scientific Computing,  
University of Warwick, Coventry, CV4 7AL, UK.  
E-mail: david.cheung@warwick.ac.uk

February 9, 2009

Using dissipative particle dynamics simulations the relationship between molecular architecture and phase behaviour in model hairy rod polymers is studied. In agreement with experimental and theoretical studies the phase behaviour is controlled by changes to the molecular structure, particularly the sidechain length and density, and the molecular interactions. For dense sidechains a lamellar structure is found, which becomes an inverted cylindrical phase when the sidechain density is lowered. The ordered phases become more stable on increasing sidechain length and on increasing the repulsion strength between the backbone and sidechains. In the absence of torsional potentials the structures are double-walled, i.e. layers are two polymer backbones thick, while single-walled structures are observed for polymers with torsional potentials.

## 1 Introduction

Hairy rod polymers [1] which consist of a rigid, typically conjugated, backbone with flexible side-chains form an interesting and technologically important class of copolymers. Originally interesting as structural materials, many of the common semiconducting polymers, such as the poly(3-alkylthiophene)s [P3ATs] and polyfluorenes (Fig. 1) fall into this category. Examples of hairy-rod polymers also include biomacromolecules, such as alkylesters of poly( $\alpha$ ,L-glutamate) [PLGA] [2], which serve as models of membrane proteins. In common with other block copolymers their phase behaviour results from microphase separation, in this case driven by the incompatibility between the rigid backbone and flexible sidechains.

One of the main driving forces behind the interest in semiconducting, hairy rod polymers is their ease of processing [3]. Typically such systems self-assemble out of solution into a range of morphologies, with typical examples being lamellar or hexagonal (cylindrical) phases [4]. The morphologies formed play an important role in determining the charge transport characteristics [5], for example P3ATs form a lamellar structure which leads to two-dimensional charge transport in the layers, with little charge transfer perpendicular to these [6]. The charge transport in semiconducting polymers is also affected by other aspects of the morphology, such as the formation of crystalline and amorphous regions [7]. Due to the interest in using hairy-rod type polymers in electronic and other applications, understanding the relation between the molecular structure and morphology is a matter of great interest, and by studying the relationship between polymer architecture and phase behaviour for simple generic models this work presents an initial contribution to this.

The relation between the architecture and morphology in hairy rod polymers has been investigated using a variety of experimental and theoretical methods. X-ray diffraction and thermal analysis on poly(3-alkylthiophene)s have shown that these form a lamellar structure for sufficiently long sidechains (four or more carbons) [8, 9]. Poly(*p*-phenylene) derivatives have also been shown to form lamellar phases for sufficiently long flexible chains [10]. As well as lamellar phases, cylindrical phases have been observed in polyfluorene derivatives [11], while lamellar and inverted cylindrical phases have been observed for rigid-rod polyesters [12, 13]. Flory theory [14] has been used to study the phase behaviour of hairy rods, primarily to study the nematic-isotropic transition in these systems [15, 16]. More recent theoretical studies [17] have determined the phase diagram as a function of side-chain length and temperature; for short side-chains a lamellar phase was found, whereas for longer side-chains two cylindrical phases, with either single or multiple polymer chains in each cylinder, were found

In contrast to the wealth of experimental and theoretical studies, hairy rod polymers have largely been neglected by simulation. The large length and timescales involved in the self-assembly of hairy-rod polymers makes atomistic simulations impractical. Such simulations have been used to study the microstructure of hairy-rod polymers, particular in the crystalline phase [18, 19, 20, 21]. Atomistic simulations have also been used to probe the microstructure and short time dynamics of melts of hairy-rod oligomers [22, 23]. Simulations using simplified, generic potentials may be used to study larger-scale morphologies, for example micelle formation in hairy-rod polyelectrolytes [24]. Recently, dissipative particle dynamics (DPD) [25] has emerged as an especially useful method for studying the rheology and self-assembly in polymer systems. It has been applied to a number of different polymer systems, ranging from immiscible polymer blends [26] to linear [27, 26, 28] and branched copolymer melts [29] to polymer brushes [30, 31]. In this paper we present a preliminary study of the relationship between molecular architecture and phase behaviour in generic hairy-rod polymer melts. This examines both the effect of changing the molecular structure and the interaction strengths between the polymer backbone and sidechains. The paper is organized as follows. The simulation methodology and model is outlined in the next section. This is followed by a presentation of the results, first the phase behaviour as a function of the molecular structure, then the effect of changing repulsion strengths. The paper concludes with a brief presentation of its main results and a discussion of avenues of future work.

## 2 Simulation model and methodology

### 2.1 Methodology

The system is simulated using dissipative particle dynamics simulations [25]. This has been thoroughly discussed in previous publications, so will only be briefly outlined here. The system evolves according to Newton's equations of motion, with the force on a particle given by the sum of conservative, dissipative (frictional) and random forces. As has been pointed out previously [32] DPD is independent of the the form of the conservative force, which will be given in the following section. In order to correctly sample the *NVT*-ensemble the forms of the frictional and random forces are constrained by the fluctuation dissipation theorem and are given by [33]

$$\mathbf{F}_{ij}^D(\mathbf{r}_{ij}) = -\gamma w(r_{ij})^2 (\mathbf{r}_{ij} \cdot \mathbf{v}_{ij}) \hat{\mathbf{r}}_{ij} \quad (1)$$

$$\mathbf{F}_{ij}^R(\mathbf{r}_{ij}) = \sigma w(r_{ij}) \zeta \hat{\mathbf{r}}_{ij} / \sqrt{\delta t} = -\mathbf{F}_{ji}^R(\mathbf{r}_{ji}) \quad (2)$$

where  $\mathbf{r}_{ij}$  and  $\mathbf{v}_{ij} = \mathbf{v}_i - \mathbf{v}_j$  are the separation vector and relative velocities of particles  $i$  and  $j$ ,  $r_{ij}$  is the interparticle distance,  $\hat{\mathbf{r}}_{ij} = \mathbf{r}_{ij}/r_{ij}$ , and  $\delta t$  is the integration timestep.  $\zeta$  is a random number of 0 mean and unit variance. The parameters damping constant  $\gamma$  and the

noise strength  $\sigma$  are related by  $\sigma^2 = 2k_B T \gamma$  and the weight function is given by [33]

$$w(r) = \begin{cases} 1 - (r/r_c) & r \leq r_c \\ 0 & \text{otherwise} \end{cases} . \quad (3)$$

In this work we use  $\gamma = 6.75$  and  $\sigma = 3.67$  [27].

The numerical integration of the equations of motion is complicated due to the velocity dependence of dissipative force. A number of sophisticated algorithms have been proposed for the integration [34]; in this paper we employ the modified velocity-Verlet algorithm of Groot *et al* [35, 27, 26]

$$\begin{aligned} \mathbf{r}_i(t + \delta t) &= \mathbf{r}_i(t) + \mathbf{v}_i(t)\delta t + \frac{1}{2m_i}\mathbf{F}_i(t)\delta t^2, \\ \tilde{\mathbf{v}}_i(t + \delta t) &= \mathbf{v}_i(t) + \lambda \frac{\mathbf{F}_i(t)}{m_i}\delta t, \\ \mathbf{F}_i(t + \delta t) &= \mathbf{F}_i(\mathbf{r}_i(t + \delta t), \tilde{\mathbf{v}}_i(t + \delta t)), \\ \mathbf{v}_i(t + \delta t) &= \mathbf{v}_i(t) + \frac{1}{2m_i}(\mathbf{F}_i(t) + \mathbf{F}_i(t + \delta t))\delta t \end{aligned} \quad (4)$$

where  $m_i$  is the mass of the  $i$ th particle, with  $m_i = 1$ .  $\lambda$  is an adjustable parameter that minimizes fluctuations in the instantaneous temperature [34]. In common with previous work, good agreement between the target and instantaneous temperatures was found for  $\lambda = 0.65$ . A timestep of  $\delta t = 0.05\tau$ , where  $\tau = r_c \sqrt{m/k_B T}$ , is used and the simulation runs were of up to  $5 \times 10^6$  timesteps.

## 2.2 Simulation model

The simulated systems consist of monodisperse polymers, containing 24000 DPD beads with a number density of  $\rho r_c^3 = 3.0$ . The monomer structure may be generically described as  $A_m B_n$ , where  $m$  and  $n$  are number beads in the backbone and sidechain respectively (with  $m = 1, 2$  and  $n = 1, 2, 3$  studied), as illustrated in Fig. 2. For the  $A_1 B_n$  polymers, chains of 20 monomers were studied, for the  $A_2 B_n$  polymers the chains consisted of 10 monomers, giving the same overall length in both cases.

The forces acting on the beads may be separated into bonded and nonbonded forces. The nonbonded forces are given by a soft repulsive interaction, which has the usual form [25]

$$\mathbf{F}_{12}^N = a_{ij} w(r_{12}) \hat{\mathbf{r}}_{12} \quad (5)$$

where  $w(r)$  is given by Eq. 3. Following Groot and Warren [35] the repulsive strength for like particles is  $a_{AA} = a_{BB} = 25\epsilon$ , while the repulsion between unlike particles  $a_{AB}$  was varied between  $37\epsilon - 75\epsilon$ . The energy unit  $\epsilon$  is also used to define a reduced temperature  $T^* = k_B T / \epsilon$ . It should be noted that in this paper we are interested in modelling the behaviour of a generic hairy-rod polymer, rather than studying a specific molecular system. The use of such soft interactions is also unlikely to accurately model the details of polymer crystallization and hence the microcrystalline structures observed in polymers such as the P3ATs [7]. Rather the aim is to study the mesophases formed between the solid phases and melts of these polymers.

The bonded interactions are a combination of bond stretches and bond angle bends

$$\mathbf{F}_i^{bond} = \sum_{j=1}^{N_{bonds}} -\nabla_i \left\{ \frac{1}{2} k_r (r_j - r_j^{eq})^2 \right\} = -k_r (r_j - r_j^{eq}) \hat{\mathbf{r}}_j \quad (6)$$

$$\mathbf{F}_i^{angle} = \sum_{j=1}^{N_{angles}} \begin{cases} -\nabla_i \left[ \frac{1}{2} k_\theta (1 + \cos \theta_j) \right] & \text{linear} \\ -\nabla_i \left[ \frac{1}{2} k_\theta (\theta_j - \theta_j^{eq})^2 \right] & \text{harmonic} \end{cases} \quad (7)$$

where  $k_r$  and  $k_\theta$  are the bond stretch and angle bending force constants and  $r_j^{eq}$  and  $\theta_j^{eq}$  are the equilibrium bond lengths and angles. For bonds between adjacent beads  $k_r = 4k\epsilon/r_c^2$  and  $r_{ij}^{eq} = 0$ . In order to preserve the rigidity of the backbone an additional bond is added between the first and last backbone beads [36], with  $k_r = 10\epsilon/r_c^2$  and  $r_j^{eq} = 15.2r_c$ .  $k_\theta = 20k_B T$  for all angles, with the linear form being used for all angles apart from AAB angles, which use the harmonic form with  $\theta_j^{eq} = 90^\circ$ .

### 3 Results and discussion

We first study the morphologies formed for  $A_1B_1$  hairy rod polymers, using the original Groot-Warren interaction parameters ( $a_{AB} = 37\epsilon$ ). Shown in Fig. 3 are representative snapshots showing the morphologies formed for temperatures ranging from  $T^* = 1$  to  $T^* = 0.5$ . At high temperatures  $T^* \geq 0.75$  the system forms a disordered, isotropic phase. On decreasing temperature ( $T^* \leq 0.70$ ) a transition to a lamellar phase is observed, with the polymer backbones lying in the lamellar planes. More information on the structure may be found from the radial distribution functions (RDF), shown in Fig. 4. For temperatures above  $T^* = 0.75$  all three RDFs [ $g_{AA}(r)$ ,  $g_{AB}(r)$ , and  $g_{BB}(r)$ ] are similar, with a peak at about  $r \approx 0.72r_c$ . There is no other noticeable structure in  $g_{AA}(r)$  and  $g_{BB}(r)$ , while  $g_{AB}(r)$  has a second peak at  $r \approx 1.5r_c$ . In the lamellar phase ( $T^* \leq 0.70$ ) more structure is present. For  $g_{AA}(r)$  and  $g_{BB}(r)$  the peak at  $r \approx 0.72r_c$  grows, while the peak in  $g_{AB}(r)$  decreases, indicating a significant degree of segregation between the backbone and sidechain beads. The RDFs also show oscillations at large  $r$ , with wavelengths given by the layer spacing.

Snapshots illustrating the phase behaviour of the other polymers are shown in Figs. 5 and 6. The phase behaviour of the  $A_1B_2$  polymer is similar to the  $A_1B_1$  polymer, with a disordered phase at high temperatures and a lamellar phase at low temperatures. On increasing sidechain length the lamellar phase becomes stable at higher temperatures and the  $A_1B_3$  polymer exhibits a lamellar phase for both temperatures studied [Figs. 5(b) and 6(b)]. When the number of backbone beads in each monomer increases (i.e. the  $A_2B_n$  polymers), the ordered phase at low temperatures changes from a lamellar to an inverted cylindrical phase. In this phase the sidechains form into cylinders, with the polymer backbones in between, lying parallel to the cylinder axes. Such inverted cylindrical (or honeycomb) phases have been observed in experimental studies of hairy rod polymers such as rigid-rod polyester derivatives [12, 13], and similar structures have also been observed in bolaamphiphilic liquid crystals, from both experiment, e.g. on terphenyl derivatives [37], and simulations [38, 39]. The cylindrical ordering in these phases may be clearly seen in the structure factor (Fig. 7). For the  $A_1B_1$  polymer the structure factor peaks have a spacing  $1 : 2 : 3 : 4$  (and higher) consistent with lamellar ordering, whereas for the  $A_2B_1$  the peaks spacings are those of the cylindrical phase ( $1 : \sqrt{3} : \sqrt{4} : \sqrt{7}$ ). The dependence of the phase behaviour on the sidechain length and density is consistent with experimental studies on systems such as poly(phenylene ethynyls) [40], poly-glutamates [41], or rigid-rod polyesters [12].

The RDFs for  $T^* = 0.5$  are shown in Fig. 8. For all the structures studied the  $AA$  RDF ( $g_{AA}(r)$ ) has a peak at  $r \approx 0.72r_c$  due to the A-A bonds. The height of this peak shows substantial variation with the monomer structure, being smallest for the  $A_2B_1$  ( $\approx 1.6$ ) and largest for  $A_1B_3$  ( $\approx 4.2$ ). At larger  $r$  there are periodic variations in  $g_{AA}(r)$  with a wavelength governed by the sidechain lengths. For the  $A_1B_1$  and  $A_2B_1$  polymers, which shows the least pronounced variation, the spacing is  $\approx 3r_c$ , for both the  $A_1B_2$  and  $A_2B_2$  polymers the spacing  $\approx 4.2r_c$ , and for the  $A_1B_3$   $\approx 5.5r_c$ .  $g_{BB}(r)$  also has a peak at  $r \approx 0.72r_c$  (as the  $AA$  and  $BB$  interaction is identical). Variation in  $g_{BB}(r)$  at large  $r$  is significantly less pronounced than in  $g_{AA}(r)$ . For all polymer structures  $g_{AB}(r)$  has a peak at  $r \approx 0.9 - 1.0r_c$  from bonded  $AB$  pairs (the  $AB$  bond length being longer than the  $AA$  bond due to the stronger repulsion), with a broad peak

at larger  $r$ . The position of this peak goes to larger  $r$  as the side-chain length increases and is located at roughly the position of the minimum in  $g_{AA}(r)$ .

Experimental studies of hairy-rod polymer melts have observed nematic phases [10], while lamellar and cylindrical phases possess a large degree of orientational ordering. The degree of orientational ordering may be found from the order parameter,  $S$ , defined as the largest eigenvalue of the order tensor

$$Q_{\alpha\beta} = \frac{1}{N} \sum_i \left\{ \frac{3}{2} u_{i\alpha} u_{i\beta} - \frac{1}{2} \delta_{\alpha\beta} \right\} \quad (8)$$

where  $\delta_{\alpha\beta}$  is the Kronecker delta function (1,  $\alpha = \beta$  and 0 otherwise) and  $\mathbf{u}_i$  is a unit vector defining the orientation of each polymer. In this case the orientation is defined as the vector joining the first and last beads in the polymer backbone. The sum in Eq. 8 runs over all the polymers. The calculated order parameters are shown in Table 1. For  $T^* \leq 0.70$  these are all larger than 0.30, indicating a significant degree of orientational order, consistent with the lamellar phase. For all the systems studied orientational order is lacking at higher temperatures ( $T^* \geq 0.75$ ). Apart from the  $A_1B_3$  polymer, these are disordered phases. In the case of the  $A_1B_3$  polymer a lamellar phase is observed at  $T^* = 1.0$ ; the low value of the order parameter and the fact that the middle eigenvalue of the order tensor ( $S_0$ ) is significantly larger than 0 suggests that the polymer chains within each layer are well ordered but the orientation of each layer is independent of the others. It is noticeable that none of the polymers studied exhibits a nematic phase, which has been observed in DPD simulations of rigid and semi-rigid rods [42, 36]. It is possible that the transition to positionally ordered phases preempts the isotropic-nematic transition. The lack of a nematic in these systems is unlikely to be due to the molecular conformations, measured through the molecular length  $l$  (the distance between the first and last beads in the backbone) and the radius of gyration  $R_g$ , defined through

$$R_g^2 = \left\langle \frac{1}{N_{beads}} \sum_{i=1}^{N_{beads}} |\mathbf{r}_i - \mathbf{r}_{com}|^2 \right\rangle \quad (9)$$

where  $N_{bead}$  is the number of beads in the polymer and  $\mathbf{r}_{com}$  is the centre of mass position. The values of these are listed in Table 1.  $R_g$  increases slightly with side-chain length, while  $l$  remains approximately constant across the different polymer structures and decreases slightly when the temperature decreases.

With the phase morphology for the basic model established, we now examine the effect of varying the repulsion between the unlike monomers, governed by  $a_{AB}$ . This parameter may be related to the Flory-Huggins  $\chi$ -parameter by [35]

$$\chi = \frac{\alpha \rho (a_{AB} - a_{AA})}{k_B T} \quad (10)$$

where  $\alpha \approx 0.101$ . For the range of  $a_{AB}$  studied in this work,  $\chi$  ranges from 3.64 to 15.15 at  $T^* = 1$ . The values of Flory-Huggins parameters are comparable those reported for experimental systems, such as cyclohexane-polystyrene mixtures ( $\chi \approx 1 - 3$ ) [43] and alkane-toluene mixtures ( $\chi \approx 5 - 40$ ) [44].

**$A_1B_n$  Polymers.** At low temperatures  $T^* = 0.50$  the  $A_1B_1$  polymer forms a lamellar phase for all  $a_{AB}$ , which may be expected on theoretical grounds. The increased repulsion between the A and B beads leads to an increase in the layer spacing given by  $d = 2\pi/k_{max}$ , where  $k_{max}$  is the position of the first peak in the structure factor, with  $d$  increasing from  $2.8r_c$  for  $a_{AB} = 37\epsilon$  to  $3.12$  for  $a_{AB} = 75\epsilon$ . At higher temperatures, increasing the repulsion between leads to the formation of a lamellar phase due to the stronger segregation between the backbone and sidechains. The change in structure may be seen from the structure factor  $S_A(k)$  (Fig. 9).

The structure factor for  $a_{AB} = 37\epsilon$  is typical of an isotropic fluid with a single broad peak and no structure at high  $k$ . On increasing  $a_{AB}$  to  $50\epsilon$  this peak grows significantly. The lack of further peaks at higher  $k$  and a moderate order parameter ( $S \approx 0.70$ ) would suggest that this is a nematic phase, however, visual inspection of simulation snapshots (Fig. 10) suggest that this is a (poorly ordered) lamellar phase. Increasing  $a_{AB}$  further results in the appearance of peaks at higher  $k$ , with spacings corresponding to those of a lamellar phase. The appearance of lamellar layers is also clearly seen in the simulation snapshots [Fig. 10(b)].

At  $T^* = 0.5$  similar behaviour is seen for the  $A_1B_n$  polymers ( $n=2,3$ ). For the  $A_1B_2$  polymer the layer spacing increases from  $d = 4.26r_c$  to  $d = 4.75r_c$ , while for the  $A_1B_3$  polymer the spacing increases from  $d = 5r_c$  to  $d = 6.03r_c$ . For higher temperatures ( $k_B T = 1.0$ ) the  $A_1B_2$  polymer forms a lamellar phase for  $a_{AB} \geq 50\epsilon$ . The  $A_1B_3$  polymer forms a lamellar phase at  $T^* = 1$  for all values of  $a_{AB}$  considered in this work. For this polymer however, the order parameter is always relatively low (between  $\approx 0.30$  and  $\approx 0.45$ ), suggesting that the layers remain orientationally decoupled from each other.

**$A_2B_n$  Polymers.** At  $T^* = 0.50$  both the  $A_2B_1$  and  $A_2B_2$  polymers form inverted hexagonal phases for all  $a_{AB}$ . As for the lamellar phase the cylinder spacing increases with  $a_{AB}$ ; for  $A_2B_1$  it grows from  $2.72r_c$  to  $3.09$  and for  $A_2B_2$  it grows from  $4r_c$  to  $5.34r_c$ . As before increasing the  $a_{AB}$  parameter leads to the formation of the ordered, in this case inverted cylindrical phase, at  $a_{AB} \geq 60\epsilon$  for the  $A_2B_1$  polymer and  $a_{AB} \geq 50\epsilon$  for the  $A_2B_2$  polymer.

It is interesting to note that all the phases presented so far are double-walled, i.e. layers in the lamellar phase and walls in the inverted cylindrical phase are two polymer backbones thick. Experimentally both double [45] and single wall [12] morphologies have been observed. Analysis of the dihedral angles between the sidechains shows that all the sidechains for a given polymer lie on the same side of the backbone. The effect of this dihedral angle distribution on the phase behaviour may be studied by adding a torsional potential, with the force given by

$$\mathbf{F}_i^{tors} = \sum_{j=1}^{N_{tors}} -\nabla_i \left\{ \frac{1}{2} V (1 + \cos \phi) \right\} \quad (11)$$

where  $\phi$  is the dihedral angle between two adjacent AB bonds and  $V = 2\epsilon$ . When this potential is added to the  $A_1B_1$  polymer (at  $T^* = 0.5$  and with  $a_{AB} = 37\epsilon$ ) it forms the inverted hexagonal phase (Fig. 11), but in this case it is single walled. This is due to the effective decrease in the side chain density caused by these lying on either side of the polymer.

## 4 Conclusions

In this paper the relationship between the molecular architecture and the phase morphology of model hairy rod copolymers is studied using DPD simulations. In agreement with experimental and theoretical studies the phase behaviour is controlled through changes both in the monomer structure, principally the sidechain length and density, and the interaction potentials. For dense sidechains a lamellar phase is formed, while decreasing sidechain density leads to the formation of an inverted cylindrical phase. In both cases the stability of the phases are increased by increasing sidechain length and repulsion between the backbone and sidechain beads. In the absence of a torsional potential the polymers form double-walled structures with the sidechains lying on the same side of the backbone. Adding an explicit torsional potential to force the side chains to lie on opposite sides of the polymer causes a change in the phase behaviour due to an effective decrease in the sidechain density, although the resulting phases are single-walled.

Unlike in experimental studies, a nematic phase is not observed in any of the systems considered in this work. Nematic phases have been observed in DPD simulations [36] and it is likely that in the systems studied the nematic window is vanishingly small or that translational ordering preempts the formation of the nematic phase.

This work represents an initial step in the study of the relationship between molecular structure and phase behaviour and morphology in hairy-rod polymers. Future work will study the phase behaviour of polydispersity and polymer blends or composites, which are of great interest in polymer photovoltaic applications. The generic parameters used in this work may be replaced by those parameterised against real systems [46]. In order to study the assembly of microcrystalline structures found in hairy-rod polymers at room temperatures, Lennard-Jones type potentials [32] may be used for some or all of the nonbonded interactions. However, such systems are much slower to reach equilibrium, so much longer simulations and the use of sophisticated techniques such as parallel tempering [47] may be required.

## Acknowledgements

This work was supported by UK EPSRC. The computational resources for this work were provided by the Centre for Scientific Computing, University of Warwick.

## References

- [1] M. Ballauf, *Angew. Chem.*, 1989, **28**(3), 253–267.
- [2] S. M. Yu and D. A. Tirrell, *Biomacromolecules*, 2000, **1**(3), 380–382.
- [3] H. Sirringhaus, T. Kawase, R. H. Friend, T. Shimoda, M. Inbasekaran, W. Wu, and E. P. Woo, *Science*, 2000, **290**(5499), 2123–2126.
- [4] M. Knaapila, R. Stepanyan, B. P. Lyons, M. Torkkeli, and A. P. Monkman, *Adv. Funct. Mater.*, 2006, **16**(5), 599–609.
- [5] D. L. Cheung and A. Troisi, *Phys. Chem. Chem. Phys.*, 2008, **10**(38), 5941–5952.
- [6] H. Sirringhaus, P. J. Brown, R. H. Friend, M. M. Nielsen, K. Bechgaard, B. M. W. Langeveld-Voss, A. J. H. Spiering, R. A. J. Janssen, E. W. Meijer, P. Herwig, and D. M. de Leeuw, *Nature*, 1999, **401**(6754), 685–688.
- [7] R. J. Kline and M. D. McGehee, *Polymer Rev.*, 2006, **46**(1), 27–45.
- [8] M. J. Winokur, P. Wamsley, J. Moulton, P. Smith, and A. J. Heeger, *Macromolecules*, 1991, **24**(13), 3812–3815.
- [9] S.-A. Chen and J.-M. Ni, *Macromolecules*, 1992, **25**(23), 6082–6089.
- [10] T. F. McCarthy, H. Witteler, T. Pakula, and G. Wegner, *Macromolecules*, 1995, **28**(24), 8350–8362.
- [11] M. Knaapila, B. P. Lyons, K. Kisko, J. P. Foreman, U. Vainio, M. Mihaylova, O. H. Seeck, L.-O. Plsson, R. Serimaa, M. Torkkeli, and A. P. Monkman, *J. Phys. Chem. B*, 2003, **107**(45), 12425–12430.
- [12] J. Watanabe, N. Sekine, T. Nematsu, H. Sone, and H. R. Kricheldorf, *Macromolecules*, 1996, **29**(13), 4816–4818.
- [13] K. Fu, N. Sekine, M. Sone, M. Tokita, and J. Watanabe, *Polymer J.*, 2002, **34**(4), 291–297.
- [14] P. J. Flory, *Principles of Polymer Chemistry*, Cornell University Press, Ithaca, 1971.
- [15] M. Ballauf, *Macromolecules*, 1986, **19**(5), 1366–1374.
- [16] M. Ballauf, *J. Polym. Sci. B*, 1987, **25**(4), 739–747.
- [17] R. Stepanyan, A. Subbotin, M. Knaapila, O. Ikala, and G. ten Brinke, *Macromolecules*, 2003, **36**(10), 3758–3763.
- [18] J. Corish, D. E. Feeley, D. A. Morton-Blake, F. Bénérière, and M. Marchetti, *J. Phys. Chem. B*, 1997, **101**(48), 10075–10085.
- [19] H. Xie, J. Corish, and D. A. Morton-Blake, *Synth. Met.*, 2000, **113**(1-2), 65–72.
- [20] H. Xie, S. O’Dwyer, J. Corish, and D. A. Morton-Blake, *Synth. Met.*, 2001, **122**(2), 287–296.
- [21] S. O’Dwyer, H. Xie, J. Corish, and D. A. Morton-Blake, *J. Phys. Cond. Mat.*, 2001, **13**(10), 2395–2410.

- [22] H.-C. Yang, C.-Y. Hua, M.-Y. Kuo, Q. Huang, and C.-L. Chen, *ChemPhysChem*, 2004, **5**, 373–381.
- [23] V. Marcon, N. van der Vegt, G. Wegner, and G. Raos, *J. Phys. Chem. B*, 2006, **110**, 5253–5261.
- [24] H. J. Limbach, C. Holm, and K. Kremer, *Macro. Chem. Phys.*, 2005, **206**(1), 77–82.
- [25] P. J. Hoogerbrugge and J. M. V. A. Koelman, *Europhys. Lett.*, 1992, **19**(3), 155–160.
- [26] R. D. Groot, T. J. Madden, and D. J. Tildesley, *J. Chem. Phys.*, 1999, **110**(19), 9739–9749.
- [27] R. D. Groot and T. J. Madden, *J. Chem. Phys.*, 1998, **108**(20), 8713–8724.
- [28] F. J. Martínez-Veracoechea and F. A. Escobedo, *J. Chem. Phys.*, 2006, **125**(10), 104907/1–12.
- [29] C.-I. Huang, H.-K. Fang, and C.-H. Lin, *Phys. Rev. E*, 2008, **77**(3), 031804/1–8.
- [30] S. Pal and C. Seidel, *Macrom. Theor. Simul.*, 2006, **15**(9), 668–673.
- [31] F. Goujon, P. Malfreyt, and D. J. Tildesley, *J. Chem. Phys.*, 2008, **129**(3), 034902/1–9.
- [32] T. Soddemann, B. Dünweg, and K. Kremer, *Phys. Rev. E*, 2003, **68**(4), 046702/1–8.
- [33] P. Espanol and P. Warren, *Europhys. Lett.*, 1995, **30**(4), 191–196.
- [34] I. Vattulainen, M. Karttunen, G. Besold, and J. M. Polson, *J. Chem. Phys.*, 2002, **116**(10), 3967–3979.
- [35] R. D. Groot and P. B. Warren, *J. Chem. Phys.*, 1997, **107**(11), 4423–4435.
- [36] Y. K. Levine, A. E. Gomes, A. F. Martins, and A. Polimeno, *J. Chem. Phys.*, 2005, **122**(14), 144902/1–7.
- [37] R. Kiefer, M. Prehm, B. Glettner, K. Pelz, U. Baumeister, F. Liu, X. Zeng, G. Ungar, and C. Tschierske, *Chem. Comm.*, 2008, pp. 3861–3863.
- [38] A. J. Crane, F. J. Martínez-Veracoechea, F. A. Escobedo, and E. A. Müller, *Soft Matter*, 2008, **4**(9), 1820–1829.
- [39] M. A. Bates and M. Walker, *Soft Matter*, 2009, **5**(2), 346–353.
- [40] T. Kim, L. Arnt, E. Atkins, and G. N. Tew, *Chem.-Eur. J.*, 2006, **12**(8), 2424–2427.
- [41] J. Watanabe, H. Ono, I. Uematsu, and A. Abe, *Macromolecules*, 1985, **18**(11), 2141–2148.
- [42] A. Alsunaidi, W. K. den Otter, and J. H. R. Clarke, *Phil. Trans. Roy. Soc. A*, 2004, **362**(1821), 1773–1781.
- [43] S. J. Mumby and P. Sher, *Macromolecules*, 1994, **27**(3), 689–694.
- [44] L. Vicente, C. Soto, H. Pacheco-Sánchez, J. Hernández-Trujillo, and J. M. Martínez-Magadán, *Fluid Phase Equilibria*, 2006, **239**(1), 100–106.
- [45] L. Li and D. M. Collard, *Macromolecules*, 2006, **39**(18), 6092–6097.
- [46] K. P. Travis, M. Bankhead, K. Good, and S. L. Owens, *J. Chem. Phys.*, 2007, **127**(1), 014109/1–12.
- [47] D. J. Earl and M. W. Deem, *Phys. Chem. Chem. Phys.*, 2005, **7**(23), 3910–3916.

Table 1: Top  $S_+$  and middle  $S_0$  eigvalues of the ordering tensor, radii of gyration and polymer length for  $a_{AB} = 37\epsilon$ . Uncertainties in the final digits are shown in parenthesis.

Polymer	$T^*$	$S_+$	$S_0$	$R_g / r_c$	$l / r_c$
A <sub>1</sub> B <sub>1</sub>	1.00	0.04(1)	0.00(1)	4.90(1)	15.2(4)
	0.75	0.3(1)	-0.12(7)	4.75(1)	15.1(3)
	0.70	0.94(1)	-0.45(4)	4.69(1)	15.1(3)
	0.50	0.98(1)	-0.47(5)	4.58(1)	15.0(2)
A <sub>1</sub> B <sub>2</sub>	1.00	0.09(3)	0.00(3)	4.91(1)	15.1(3)
	0.50	0.95(1)	-0.47(5)	4.61(1)	14.9(2)
A <sub>1</sub> B <sub>3</sub>	1.00	0.30(5)	0.12(5)	5.13(2)	15.2(3)
	0.50	0.83(1)	-0.36(1)	4.76(3)	15.0(2)
A <sub>2</sub> B <sub>1</sub>	1.00	0.03(1)	0.00(1)	4.88(1)	15.2(3)
	0.50	0.98(1)	-0.49(5)	4.59(1)	15.0(3)
A <sub>2</sub> B <sub>2</sub>	1.00	0.16(4)	-0.04(3)	5.05(1)	15.1(3)
	0.50	0.96(1)	-0.47(5)	4.67(2)	15.0(2)

- Fig. 1** Structures of typical hairy-rod polymers. (a) poly(3-alkylthiophene), (b) polyfurene ( $R=C_nH_{2n+1}$ ).
- Fig. 2** Structure of  $A_2B_2$  dimer.
- Fig. 3** Simulation snapshots of  $A_1B_1$  polymer (with  $a_{AB} = 37\epsilon$ ) at (a)  $T^* = 1.00$ , (b)  $T^* = 0.75$ , (c)  $T^* = 0.70$ , and (d)  $T^* = 0.50$ . Left hand column shows backbone beads, right hand column side chain beads.
- Fig. 4** Radial distribution functions for  $A_1B_1$  polymer (with  $a_{AB} = 37\epsilon$ ) at  $T^* = 1.0$  (solid line, black),  $T^* = 0.75$  (dotted line, red),  $T^* = 0.70$  (dashed line, green), and  $T^* = 0.50$  (dot-dashed line, blue).
- Fig. 5** Simulation snapshots of (a)  $A_1B_2$ , (b)  $A_1B_3$ , (c)  $A_2B_1$ , and (d)  $A_2B_2$  polymers  $T^* = 1.00$  (with  $a_{AB} = 37\epsilon$ ). Left hand column shows backbone beads, right hand column side chain beads.
- Fig. 6** Simulation snapshots of (a)  $A_1B_2$ , (b)  $A_1B_3$ , (c)  $A_2B_1$ , and (d)  $A_2B_2$  polymers  $T^* = 0.50$  (with  $a_{AB} = 37\epsilon$ ). Left hand column shows backbone beads, right hand column side chain beads.
- Fig. 7** Structure factors  $S_A(k)$  for (a)  $A_1B_1$  and (b)  $A_2B_1$  polymers at  $T^* = 0.50$  (with  $a_{AB} = 37\epsilon$ ).
- Fig. 8** Radial distribution functions for hairy rod polymers at  $T^* = 0.5$  (with  $a_{AB} = 37\epsilon$ ). Solid line (black)  $A_1B_1$  polymer, dotted line (red)  $A_1B_2$ , dashed line (green)  $A_1B_3$ , dot-dashed line (blue)  $A_2B_1$ , and double-dot-dashed line (magenta)  $A_2B_2$ .
- Fig. 9** Structure factors  $S_A(k)$  for  $A_1B_1$  polymer at  $T^* = 1.0$  with (a)  $a_{AB} = 37\epsilon$ , (b)  $a_{AB} = 50\epsilon$ , (c)  $a_{AB} = 60\epsilon$ , and (d)  $a_{AB} = 75\epsilon$ .
- Fig. 10** Simulation snapshots (backbone beads only) for  $A_1B_1$  polymer at  $T^*1.0$  with (a)  $a_{AB} = 50\epsilon$  and (b)  $a_{AB} = 75\epsilon$ .
- Fig. 11** Simulation snapshots for  $A_1B_1$  polymer at  $T^* = 0.5$  with torsional potential given by Eq. 11. Backbone beads shown on left, sidechain beads shown on right.

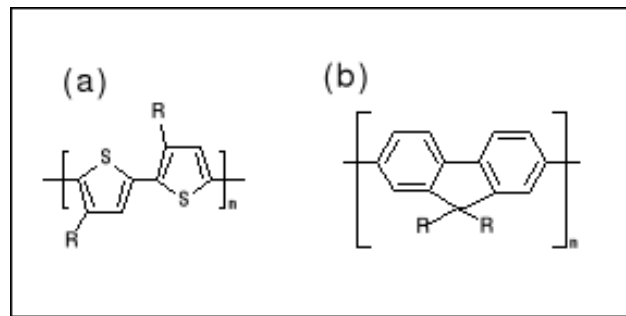


Figure 1: Structures of typical hairy-rod polymers. (a) poly(3-alkylthiophene), (b) polyfluorene ( $R=C_nH_{2n+1}$ ).

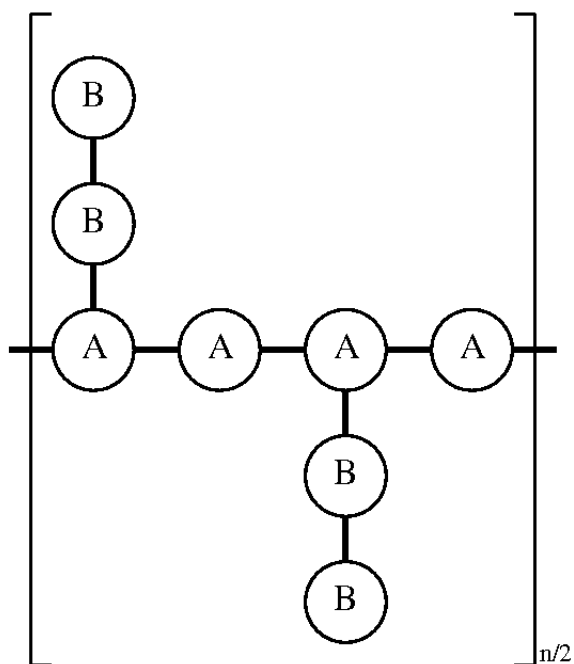


Figure 2: Structure of  $A_2B_2$  dimer

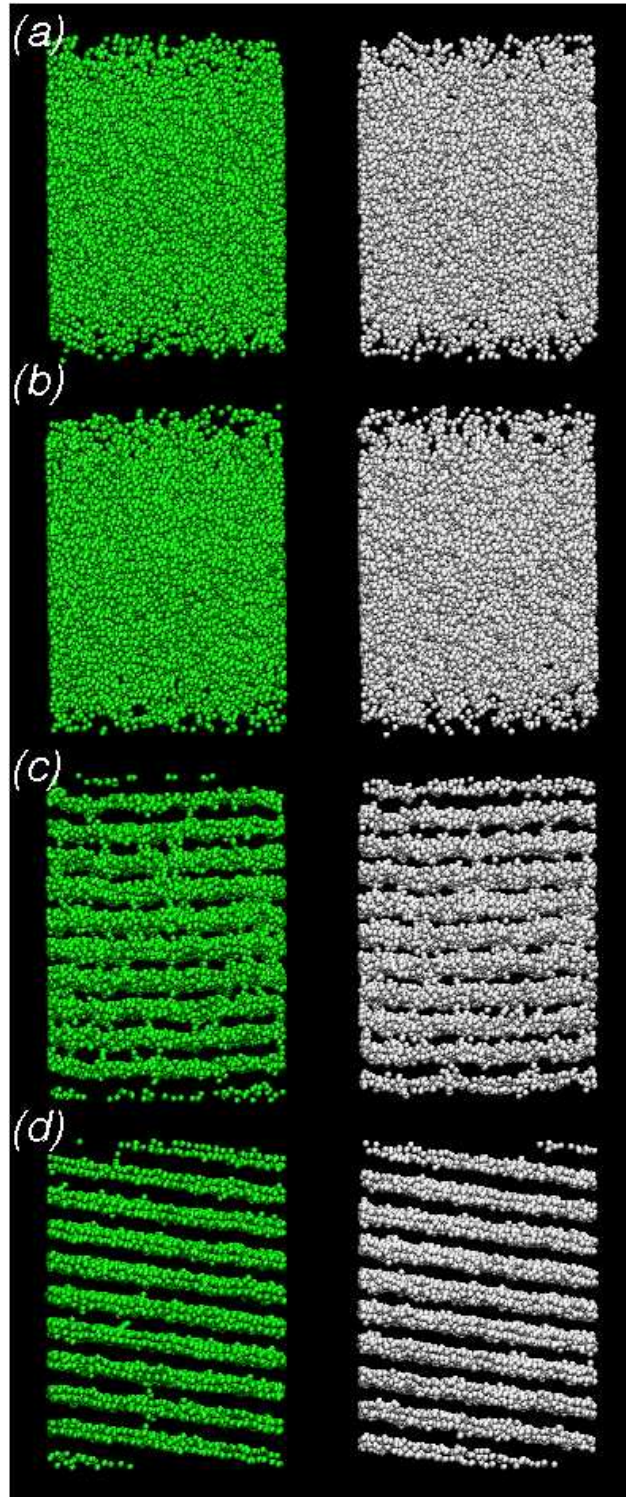


Figure 3: Simulation snapshots of  $A_1B_1$  polymer (with  $a_{AB} = 37\epsilon$ ) at (a)  $T^* = 1.00$ , (b)  $T^* = 0.75$ , (c)  $T^* = 0.70$ , and (d)  $T^* = 0.50$ . Left hand column shows backbone beads, right hand column side chain beads.

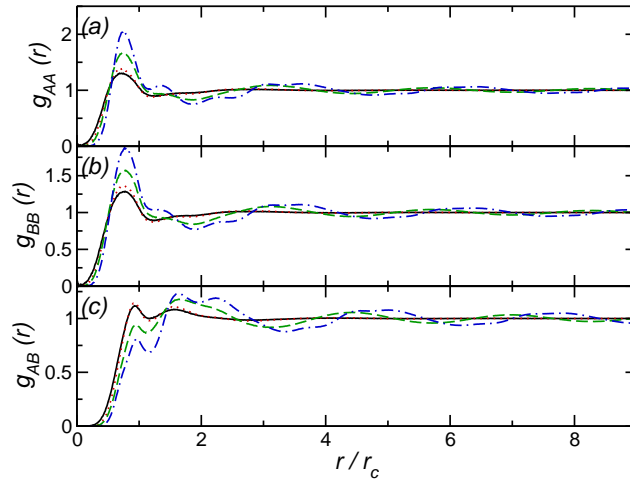


Figure 4: Radial distribution functions for  $A_1B_1$  polymer (with  $a_{AB} = 37\epsilon$ ) at  $T^* = 1.0$  (solid line, black),  $T^* = 0.75$  (dotted line, red),  $T^* = 0.70$  (dashed line, green), and  $T^* = 0.50$  (dot-dashed line, blue).

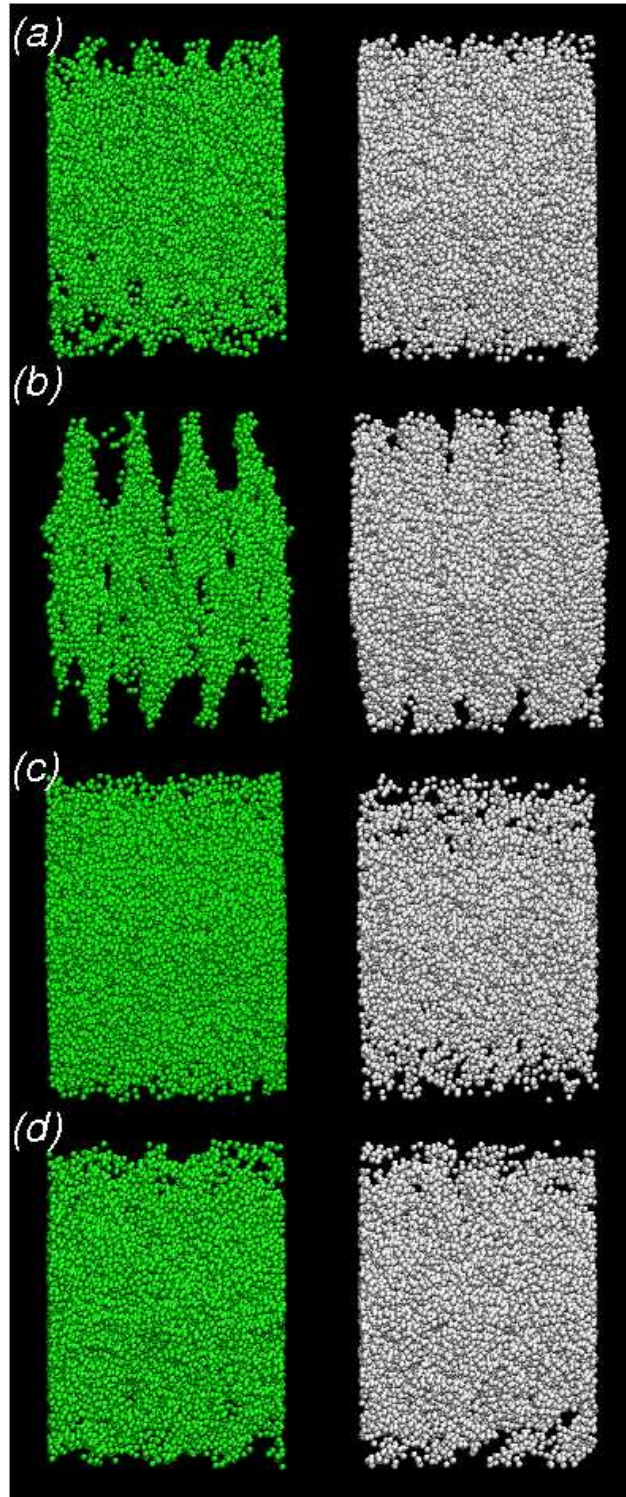


Figure 5: Simulation snapshots of (a)  $A_1B_2$ , (b)  $A_1B_3$ , (c)  $A_2B_1$ , and (d)  $A_2B_2$  polymers  $T^* = 1.0$  (with  $a_{AB} = 37\epsilon$ ). Left hand column shows backbone beads, right hand column side chain beads.

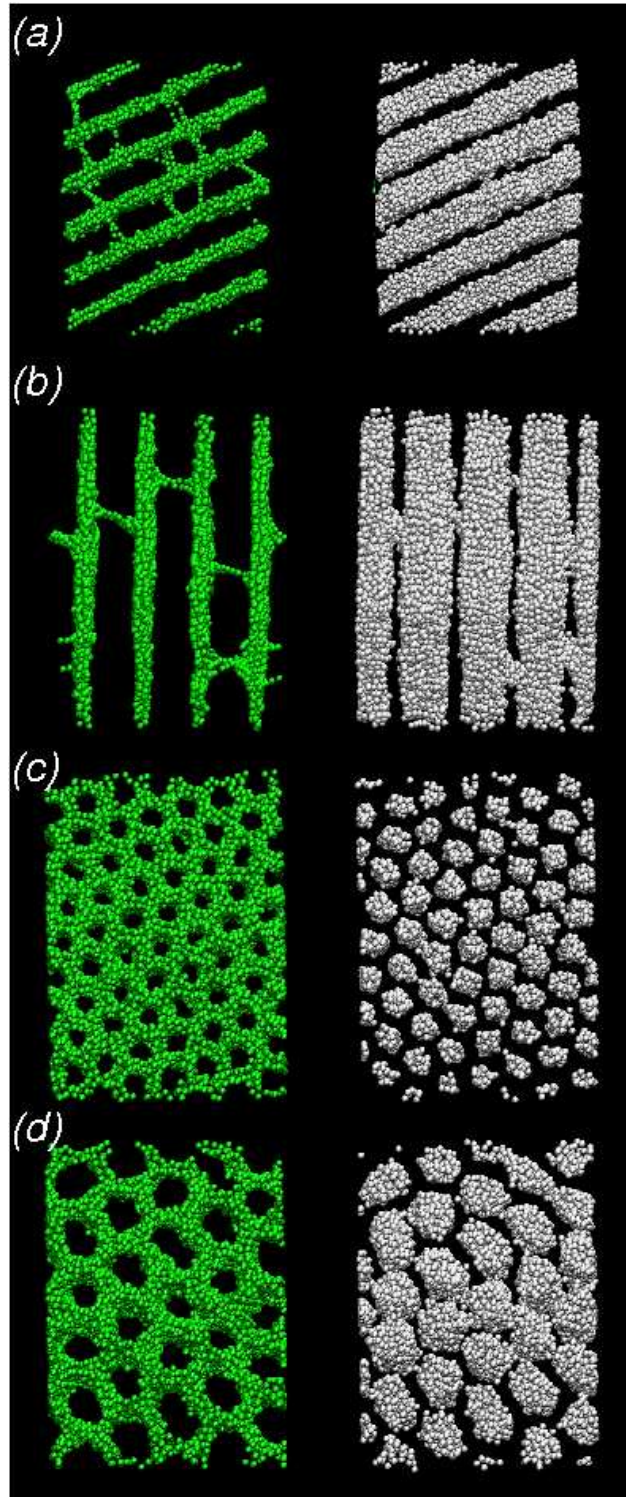


Figure 6: Simulation snapshots of (a)  $A_1B_2$ , (b)  $A_1B_3$ , (c)  $A_2B_1$ , and (d)  $A_2B_2$  polymers  $T^* = 0.5$  (with  $a_{AB} = 37\epsilon$ ). Left hand column shows backbone beads, right hand column side chain beads.

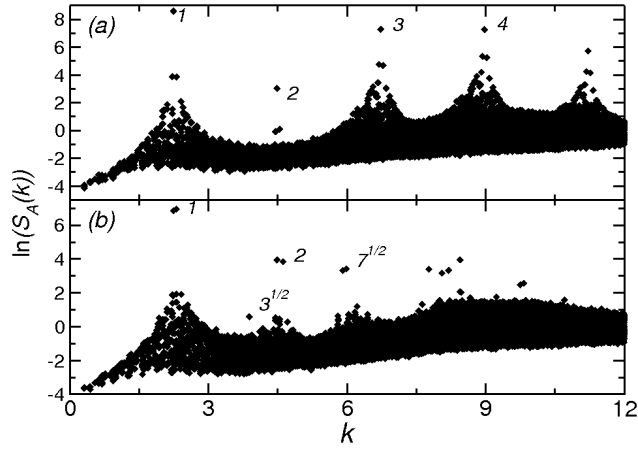


Figure 7: Structure factors  $S_A(k)$  for (a)  $A_1B_1$  and (b)  $A_2B_1$  polymers at  $T^* = 0.5$  (with  $a_{AB} = 37\epsilon$ ).

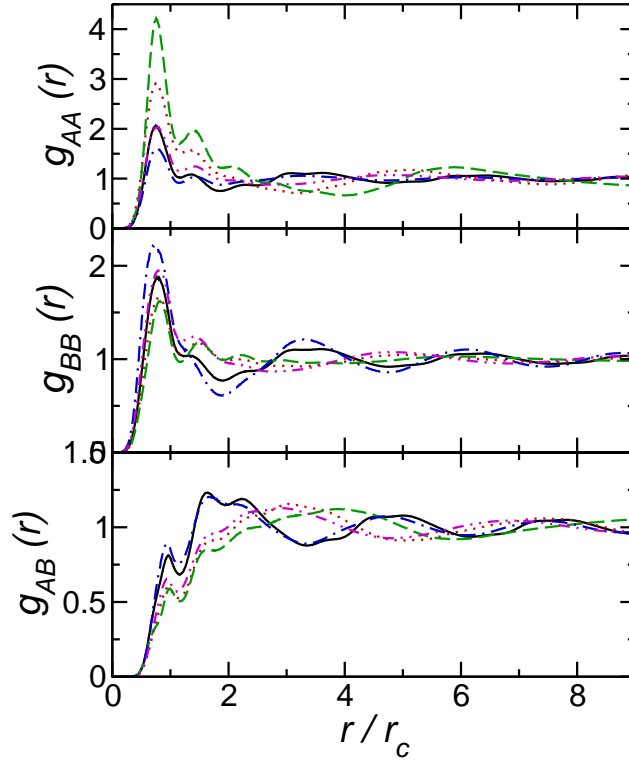


Figure 8: Radial distribution functions for hairy rod polymers at  $T^* = 0.5$  (with  $a_{AB} = 37\epsilon$ ). Solid line (black)  $A_1B_1$  polymer, dotted line (red)  $A_1B_2$ , dashed line (green)  $A_1B_3$ , dot-dashed line (blue)  $A_2B_1$ , and double-dot-dashed line (magenta)  $A_2B_2$ .

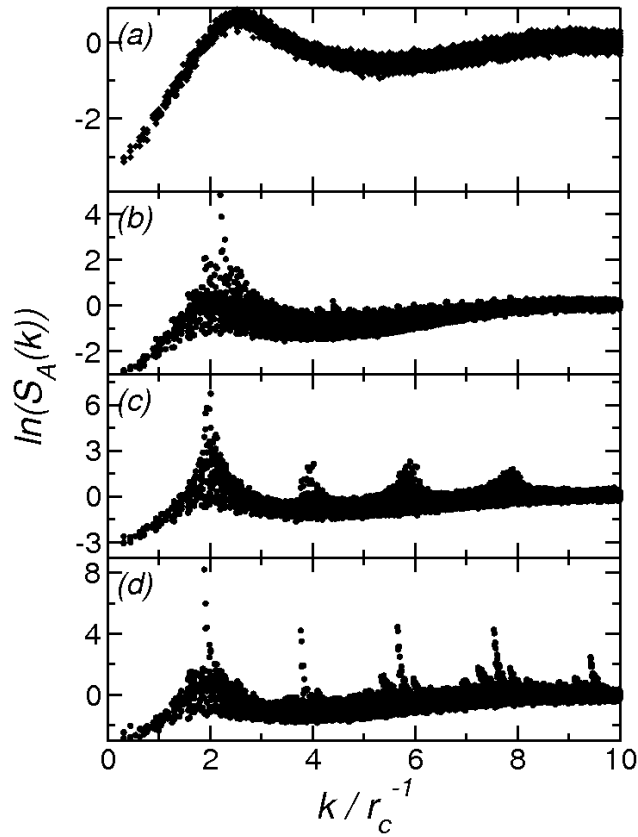


Figure 9: Structure factors  $S_A(k)$  for  $A_1B_1$  polymer at  $T^* = 1.0$  with (a)  $a_{AB} = 37\epsilon$ , (b)  $a_{AB} = 50\epsilon$ , (c)  $a_{AB} = 60\epsilon$ , and (d)  $a_{AB} = 75\epsilon$ .

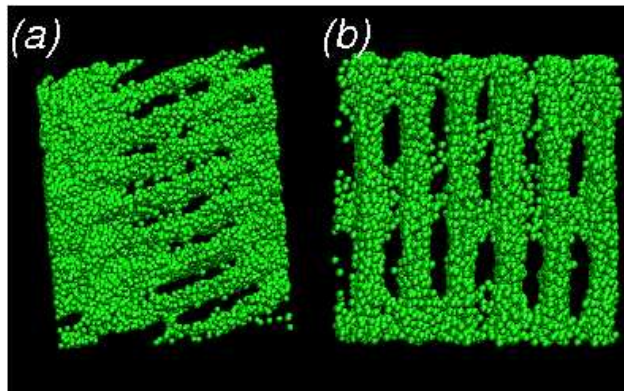


Figure 10: Simulation snapshots (backbone beads only) for  $A_1B_1$  polymer at  $T^* = 1.0$  with (a)  $a_{AB} = 50\epsilon$  and (b)  $a_{AB} = 75\epsilon$ .

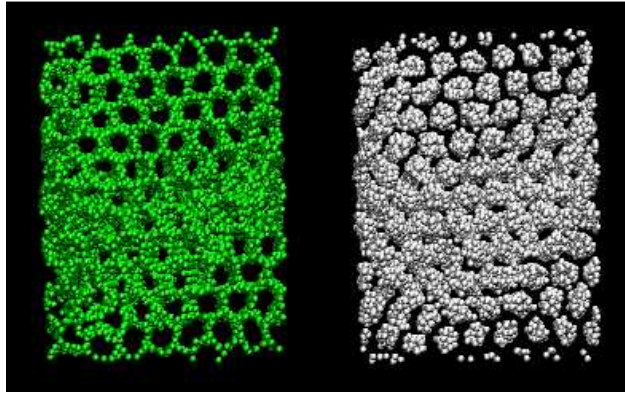


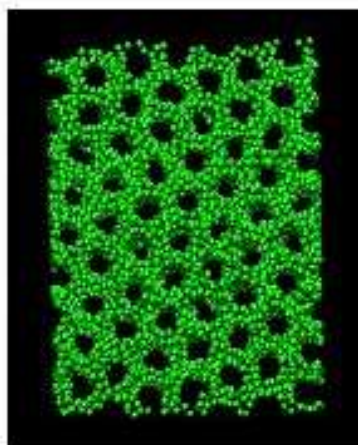
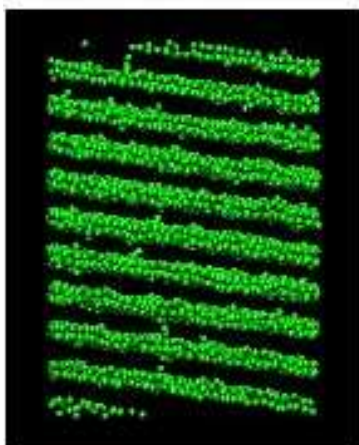
Figure 11: Simulation snapshots for  $A_1B_1$  polymer at  $T^* = 0.5$  with torsional potential given by Eq. 11. Backbone beads shown on left, sidechain beads shown on right.

## Textual Abstract

Dissipative particle dynamics simulations are used to study the phase behaviour of a model hairy-rod polymer, as the molecular structure and interactions are varied. Lamellar (left) and inverted cylindrical (right) phases are observed.

Graphical Abstract

***Backbone***



***Sidechain***

